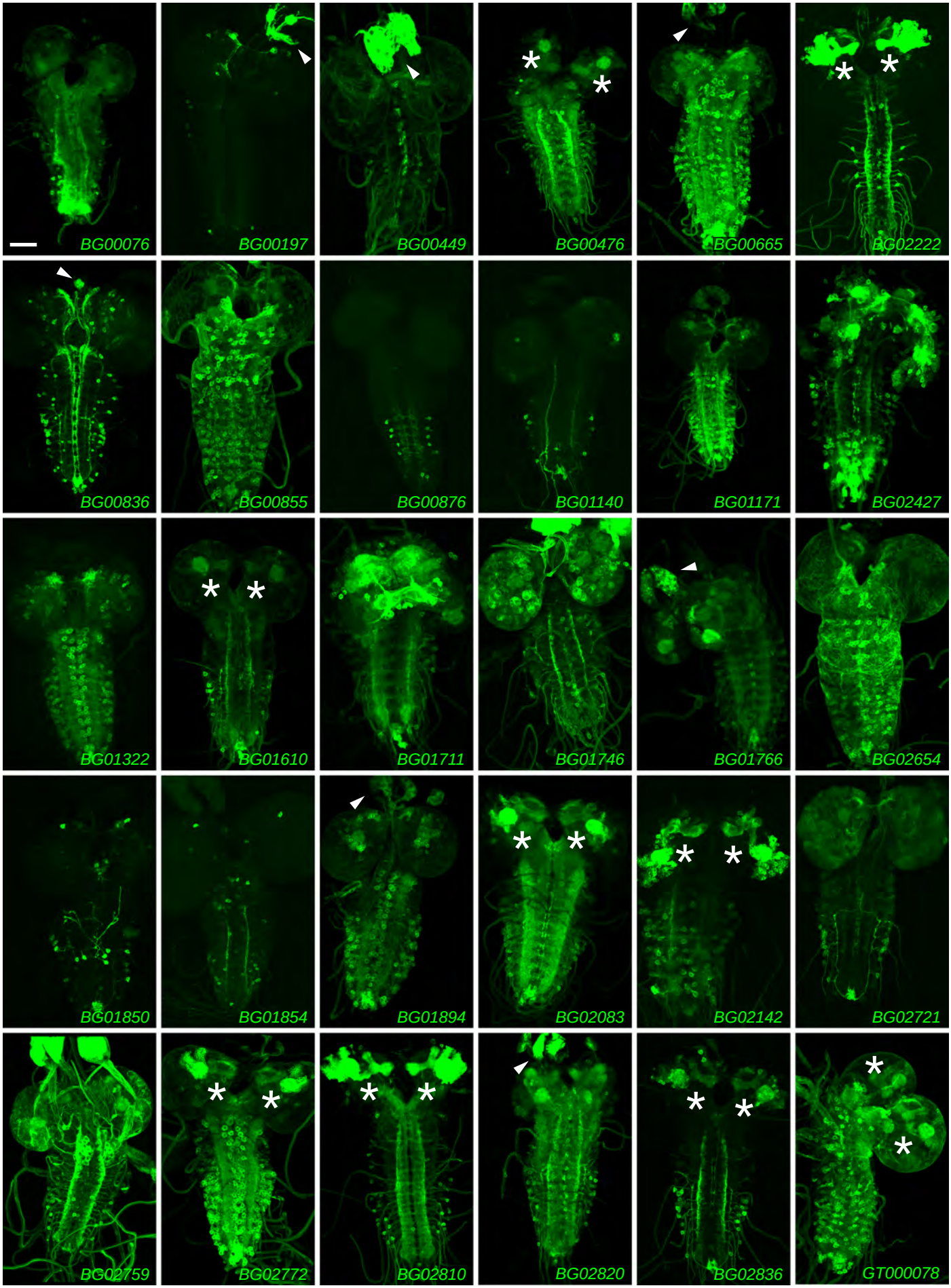

Figure S1 Reporter gene expression patterns for 30 insertions with expression in neurons. Each line was crossed to *UAS-mCD8::GFP* prior to isolation of the CNS at the wandering 3rd instar larval stage, and representative confocal z-series projections of fixed tissues are shown. Arrowheads indicate expression in the ring gland, and asterisks denote expression in the mushroom bodies. Scale bar: 50µm.

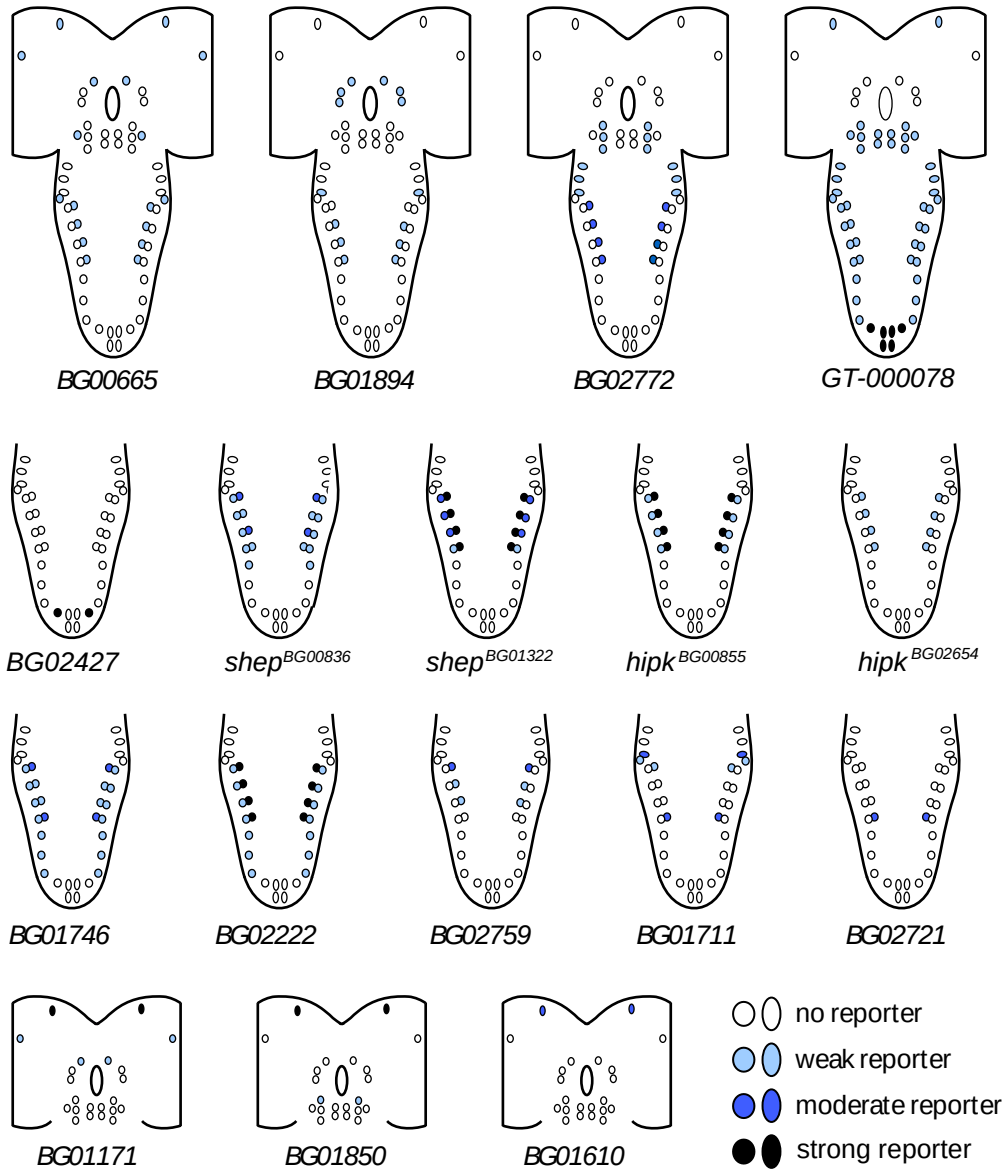

Figure S2 Patterns of splice-trap reporter gene expression in CCAP neurons in the wandering 3rd instar larval CNS. We found 17 insertions that drove expression in CCAP neurons, which are indicated with circles on the schematic CNS diagrams. The relative intensities of GFP reporter expression (mCD8::GFP, subjective scale) are indicated with different colors, and CCAP neurons with no detectable expression of the reporter are indicated with open circles. If there was no reporter expression in the brain lobes or ventral nerve cord, those regions of the CNS are not shown.

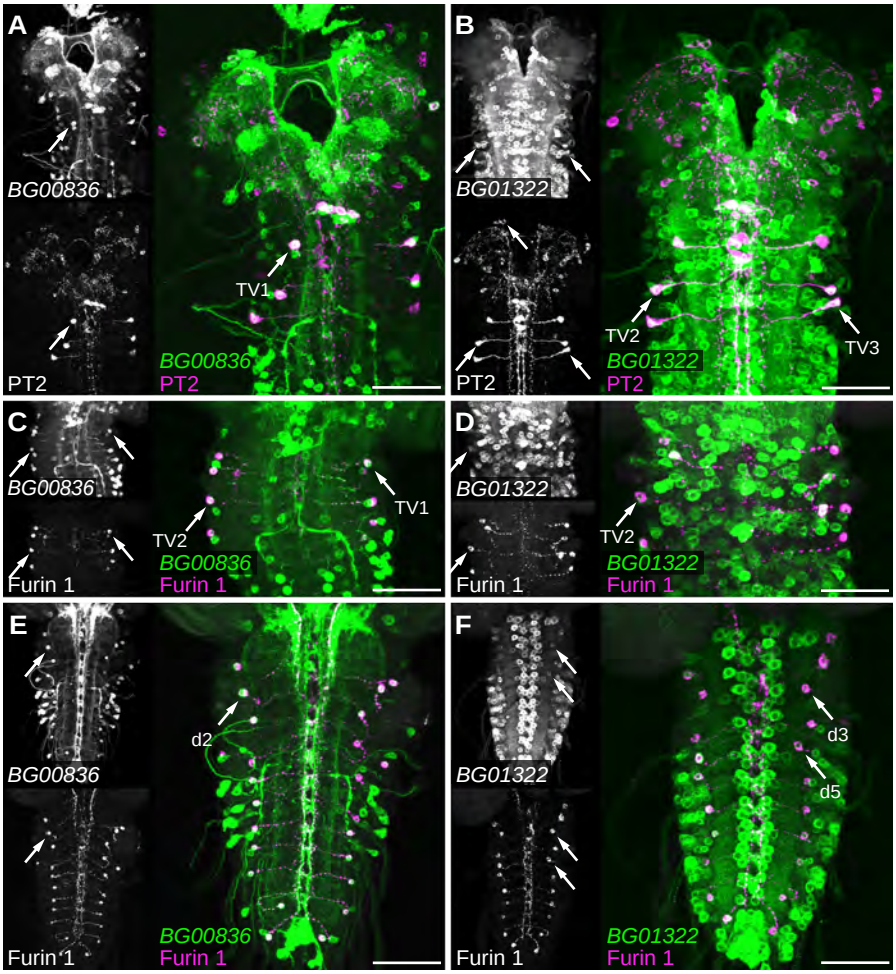

Figure S3 Reporter gene expression for the two *shep* splice-trap insertions, *BG00836* and *BG01322*, in multiple types of peptidergic neurons. (A-B) Co-localization of immunostaining with the PT2 antiserum (magenta) and mCD8::GFP reporter expression driven by *BG00836* (panel A) and *BG01322* (panel B). (C-F) Co-localization of anti-Furin 1 immunostaining (magenta) and mCD8::GFP reporter expression driven by *BG00836* (panels C and E) and *BG01322* (panels D and F). Panels C and D are ventral views of a portion of the ventral nerve cord, and panels E and F are dorsal views. Arrows: examples of colocalization of the immunosignal and reporter gene expression. Scale bars: 50 µm.

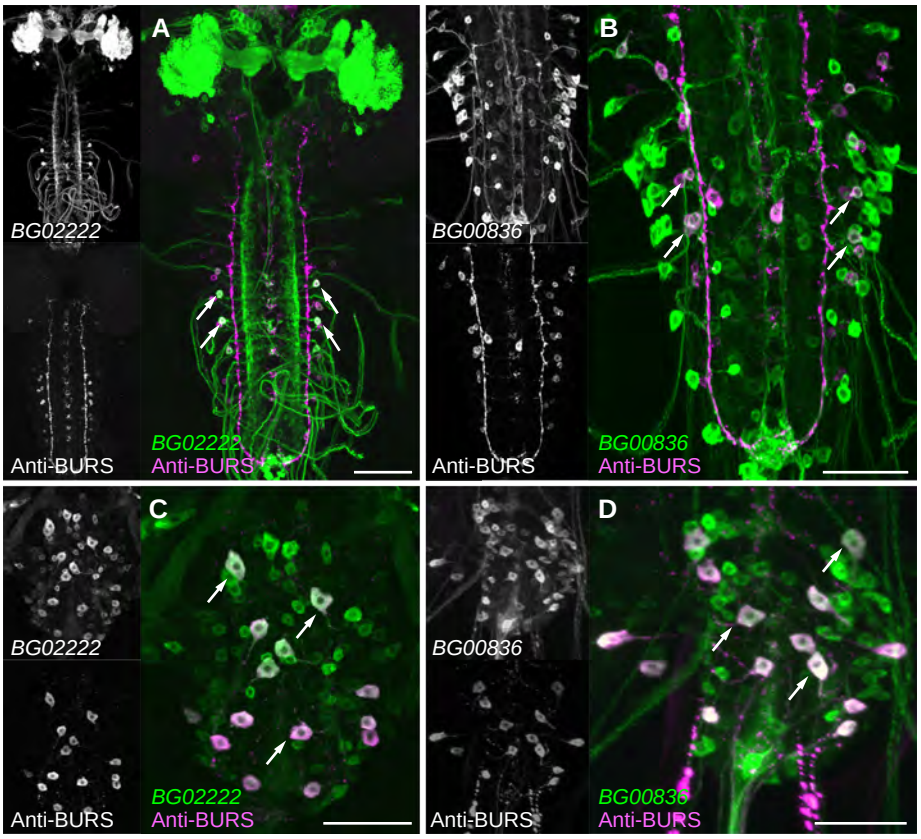

Figure S4 Selected splice-trap expression patterns that contained bursicon neurons. (A-B) Co-localization of immunostaining with an anti-BURS antiserum (magenta) and mCD8::GFP reporter expression (green) driven by *BG02222* (panel A) and *BG00836* (panel B) in wandering 3rd instar larvae. (C-D) At the P14 pharate adult stage, both *BG02222* and *BG00836* drove reporter expression in all 14 bursicon neurons in the abdominal ganglia. Arrows, examples of abdominal bursicon neurons with co-localization of the two markers. Scale bars: 50 μm.

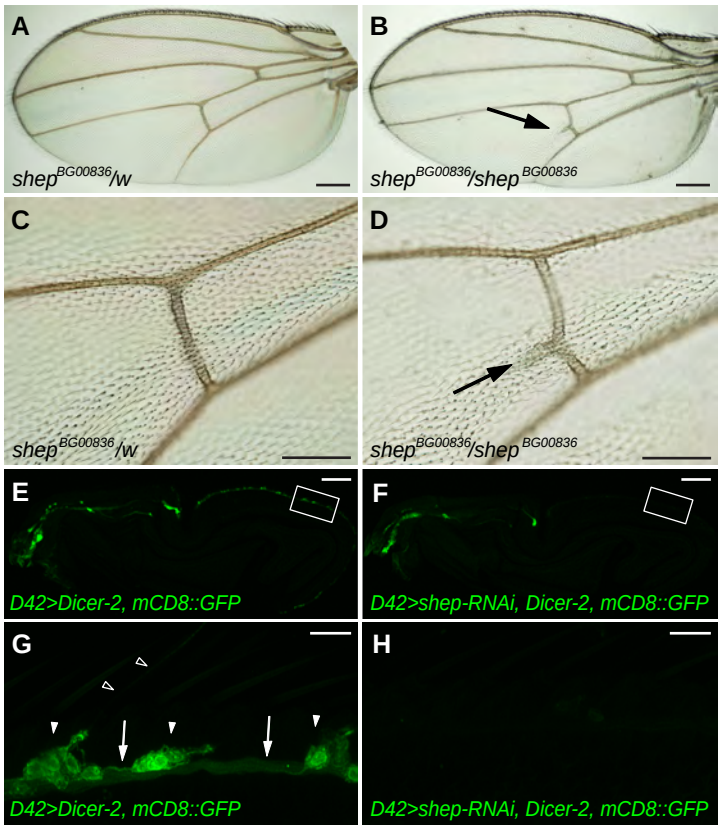

Figure S5 Loss of wing sensory neurons and appearance of ectopic wing veins following loss of *shep*. (A-D) 40% (23 out of 57) *shep*^{BG00836} homozygotes had an ectopic vein on the posterior crossvein (arrows) that was not found in *shep*^{BG00836}*/w* control flies. Panels C-D are higher magnification views of the region containing the posterior crossvein. Scale bars: A and B, 200 µm; C and D, 100 µm. (E) At the P14 pharate adult stage, sensory neurons on the wings of *D42>Dicer-2, mCD8::GFP* flies had proximal neurite projections. (F) In *shep* RNAi animals (*D42>shep-RNAi, Dicer-2, mCD8::GFP*), the proximal projections and most sensory neuron somata were absent. Scale bars: 100 µm. (G-H) Higher magnification views of the developing wing border in the highlighted box in panel E and F. Arrows, sensory neurons; Arrowheads, neurite projections of the sensory neurons; Open arrowheads, bristle neurites. Scale bars: 10 µm.

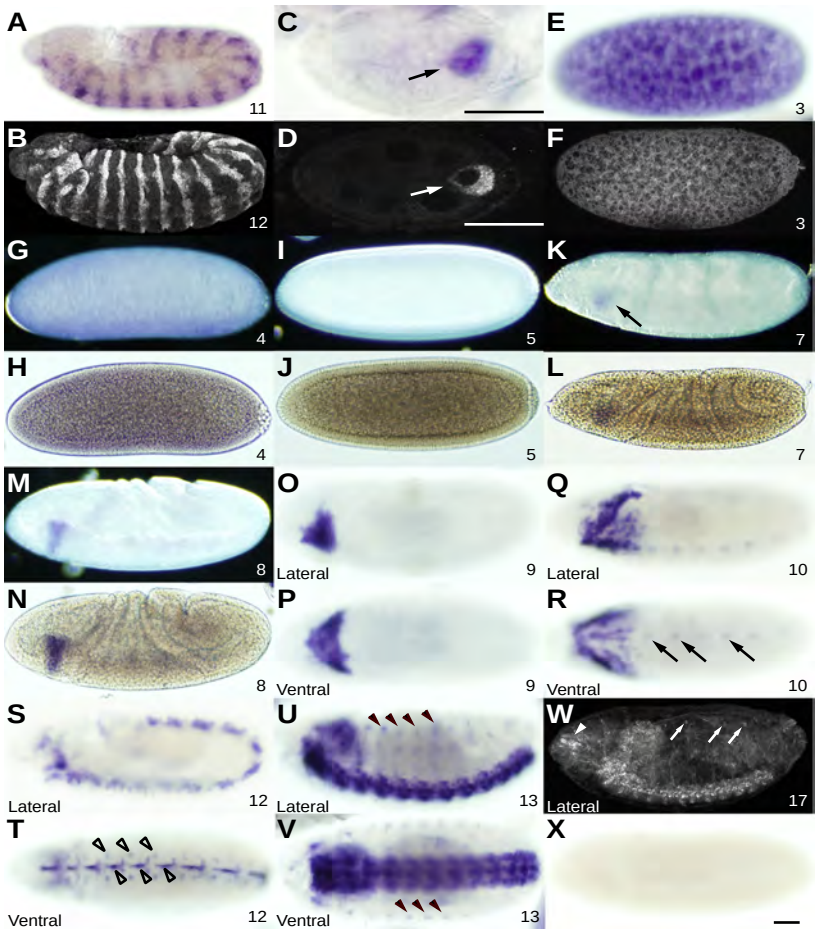

Figure S6 Embryonic *shep* mRNA and SHEP protein expression patterns. (A-B) Ectopic expression of *shep* in stage 11-12 *engrailed-Gal4/UAS-shep* embryos was detected by *in situ* hybridization (A) and immunostaining (B) with an anti-SHEP antiserum. (C-F) Expression of *shep* was detected in oocytes (arrows in panels C-D) in the ovaries of P14 stage pharate adult females and in syncytial blastoderm embryos (panels E-F) by *in situ* hybridization (blue) and immunostaining with antibodies to SHEP (gray). (G-N) Expression of *shep* in early embryonic stages detected by *in situ* hybridization. Each top-bottom pair of images shows signals from the same embryo with dark field and köhler illumination. Zygotic *shep* was first detected at stage 7 in the pro-cephalic neurogenic region (arrow, panel K). (O-V) In later embryonic stages, the expression of *shep* expanded to include the entire central and peripheral nervous systems. Each top-bottom pair of images are lateral (top) and ventral (bottom) views of the same embryos. Arrows, putative mesectoderm; open arrowheads, ventral neurogenic region; arrowheads, peripheral nervous system. (W) Anti-SHEP immunostaining produced labeling in the CNS, PNS (arrows), and the antennomaxillary complex and labral sensory complex (arrowhead). (X) Control *in situ* hybridization with the sense probe in an *Oregon R* embryo. The embryonic stage is indicated in the lower right corner of each panel. Scale bars: (C, D), 25 μm; (all other panels), 50 μm.

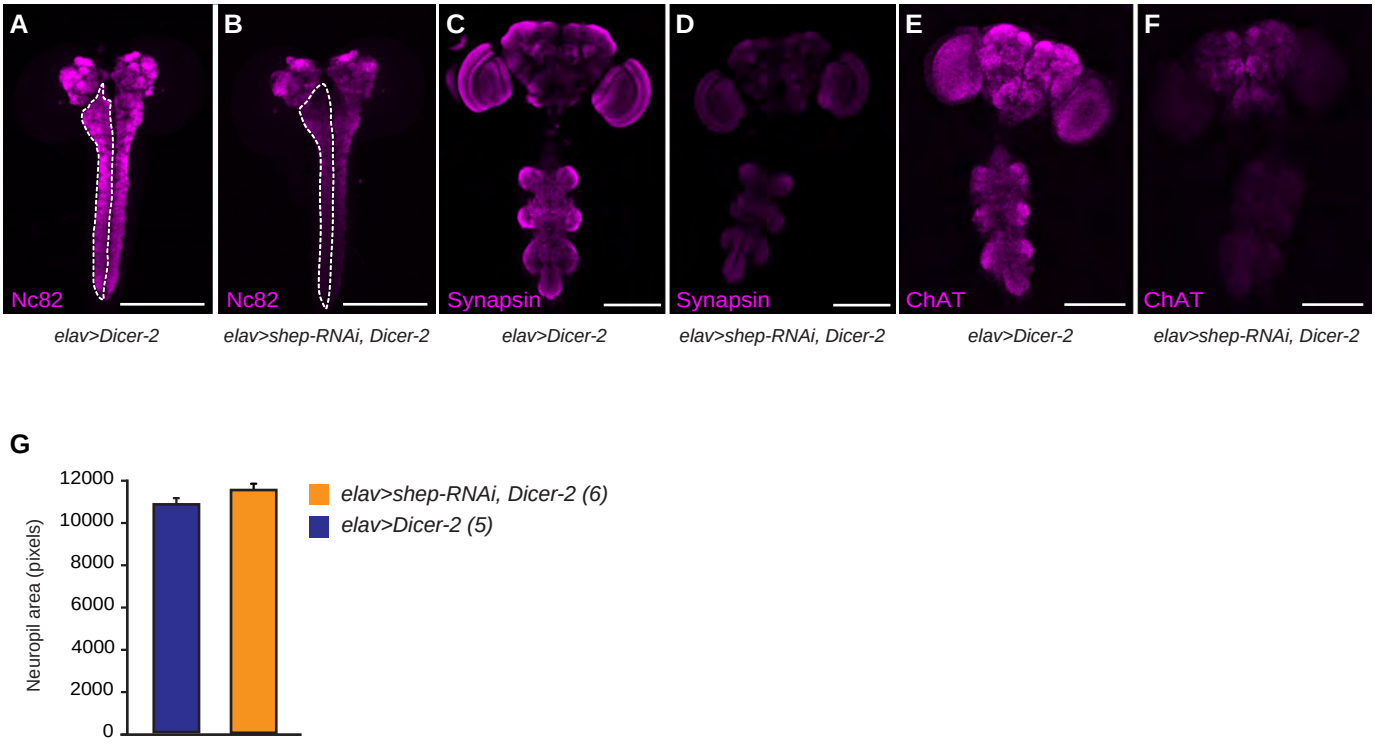

Figure S7 Loss of *shep* led to reduced levels of multiple presynaptic markers in the larval and pharate adult CNS. (A-B) Anti-nc82 immunostaining for the active zone protein Bruchpilot in wandering 3rd instar *elav>shep-RNAi, Dicer-2* larvae displayed lower signal intensity (panel B) than in *elav>Dicer-2* control larvae (panel A). (C-F) Immunostaining in P14 pharate adult CNS for Synapsin and Choline acetyltransferase (ChAT) revealed lower levels of both presynaptic markers in *shep* RNAi animals (D, F) than in *elav>Dicer-2* controls (C, E). Scale bars: 200 µm. (G) Quantification of neuropil area for the anti-nc82 immunostaining in wandering 3rd instar larvae. The ventral nerve cord neuropil area (dashed lines, panels A and B) was unchanged in *elav>shep-RNAi, Dicer-2* animals at the wandering 3rd instar stage (P=0.143, Student's t-test).

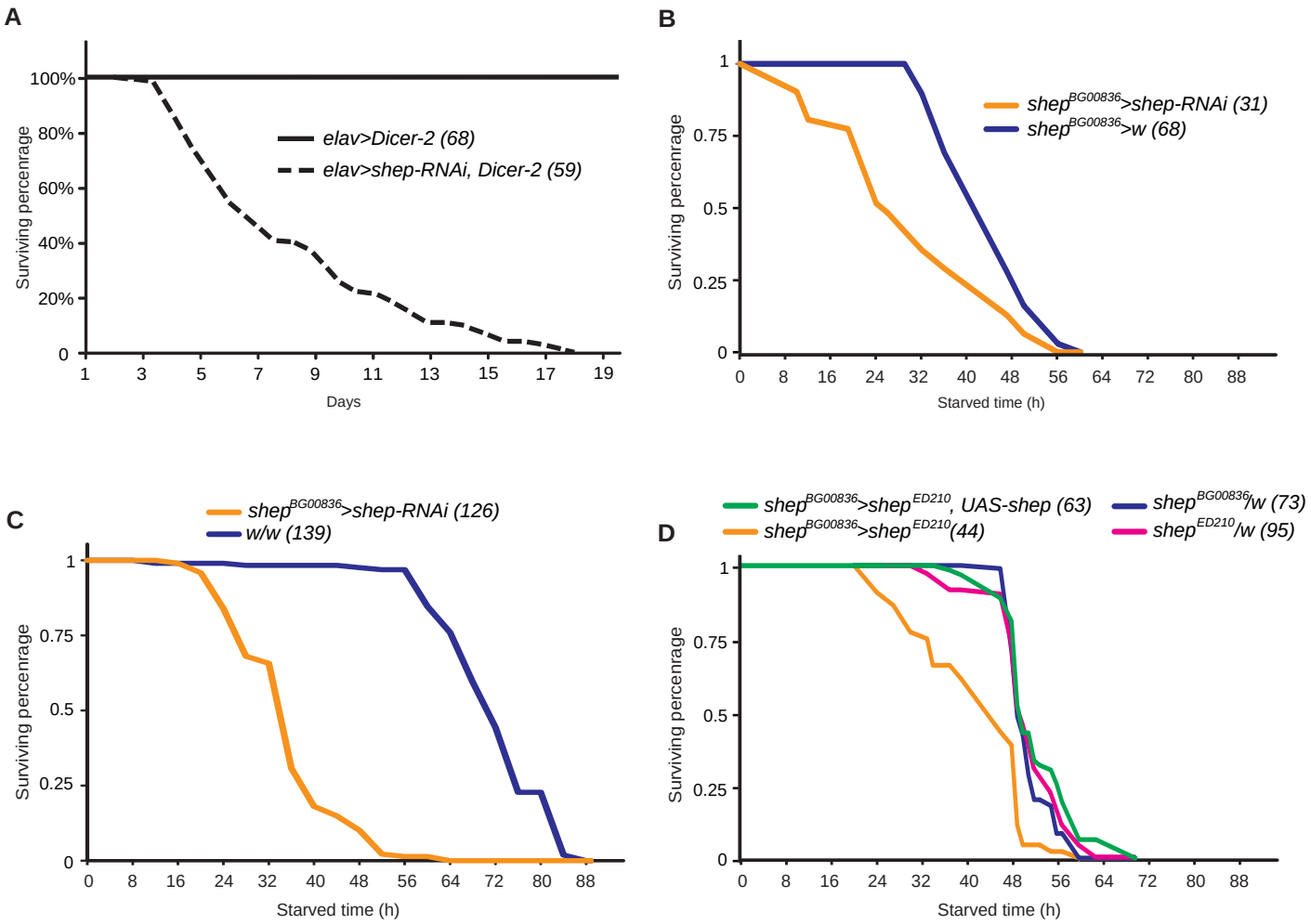

Figure S8 Loss of *shep* resulted in reduced life span. (A) Pan-neuronal *shep* RNAi led to shorter life span. The running percentage of surviving adults was plotted for *elav>shep-RNAi, Dicer-2* and *elav>Dicer-2* adult flies on regular food. (B-D) Reduced starvation resistance was detected in multiple *shep* mutants. Cumulative survival under starvation conditions was calculated (see methods) for $shep^{BG00836}$ *>shep-RNAi,* $shep^{BG00836}$ homozygotes, $shep^{BG00836}/shep^{ED210}$ mutants, and $shep^{BG00836}/shep^{ED210}$*, UAS-shep* rescue flies. In each panel, the *shep* loss-of-function genotype is labeled in orange. The results for *shep* heterozygotes are shown in blue and magenta, and the results for flies rescued with *UAS-shep* are shown in green. Sample sizes are listed in parentheses following each genotype.

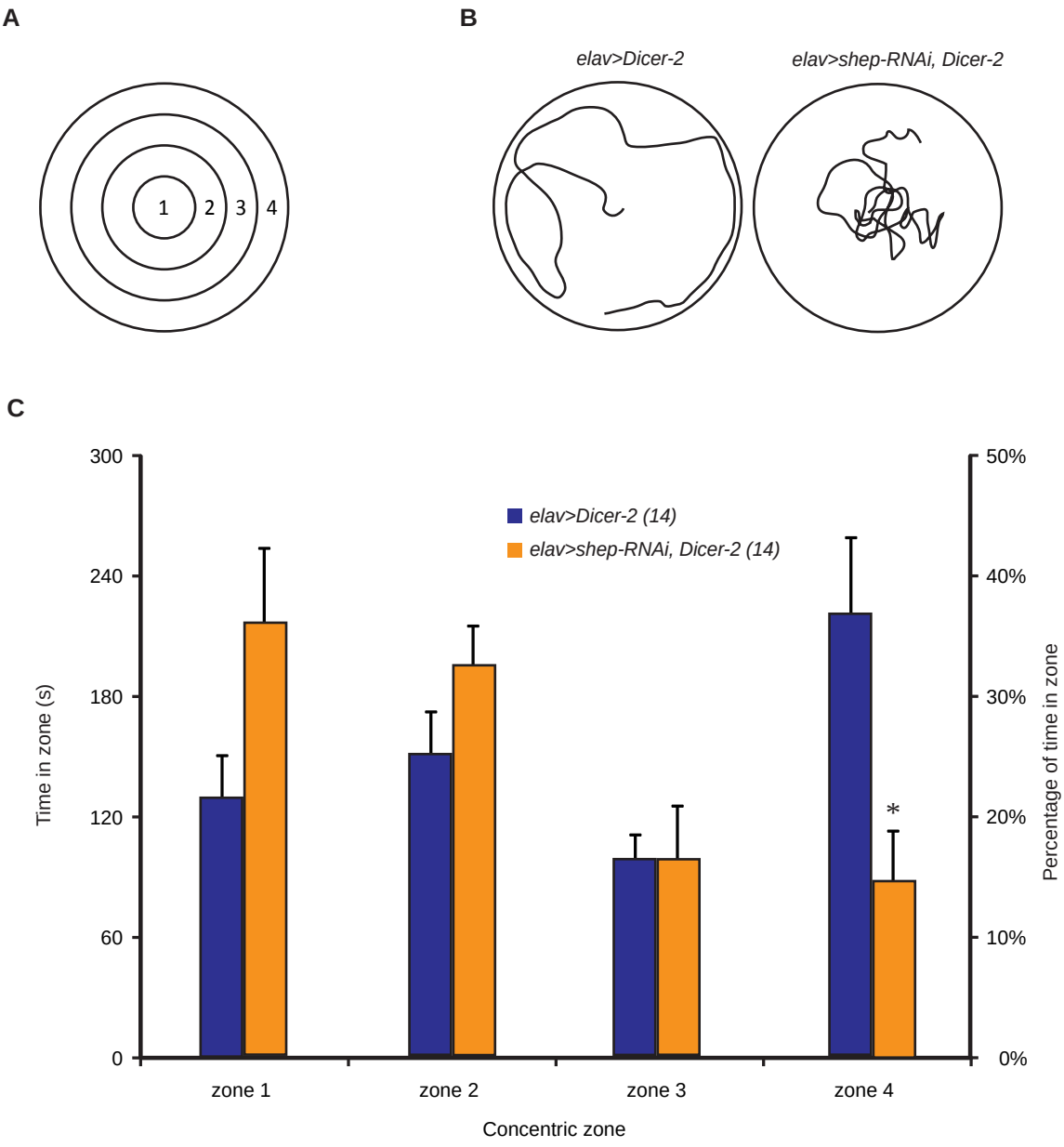

Figure S9 Pan-neuronal loss of *shep* produced larvae that remained near the center of apple-juice plates during locomotor behavior assays. (A) Apple juice-agarose plates were placed on a grid of concentric circles that defined four zones from the center to the periphery. (B) Representative 10-minute crawling trails for *elav>Dicer-2* and *elav>shep-RNAi, Dicer-2* wandering 3rd instar larvae. (C) The percentage of time spent by *elav> Dicer-2* and *elav>shep-RNAi, Dicer-2* larvae in each of the four concentric zones. The number of animals for each genotype is indicated in parentheses. *P<0.05; Separate Student's *t*-tests with Bonferroni correction were performed for each zone.

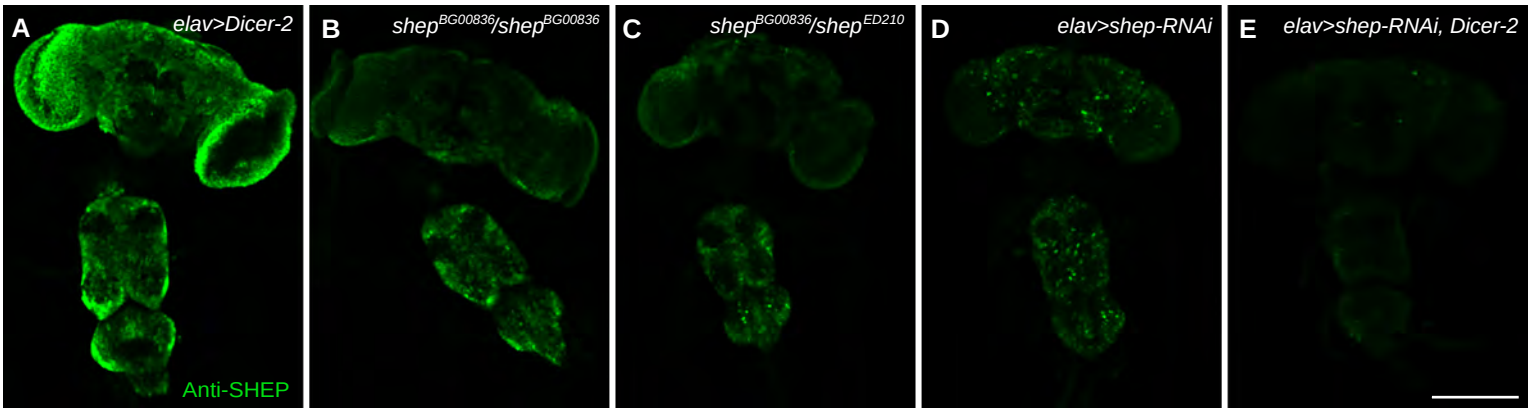

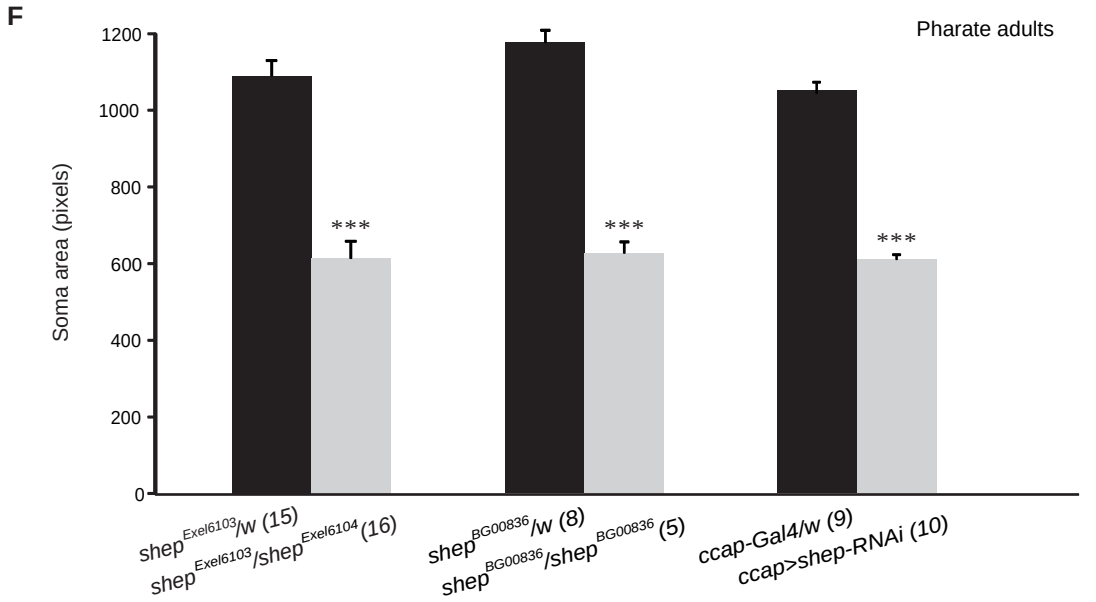

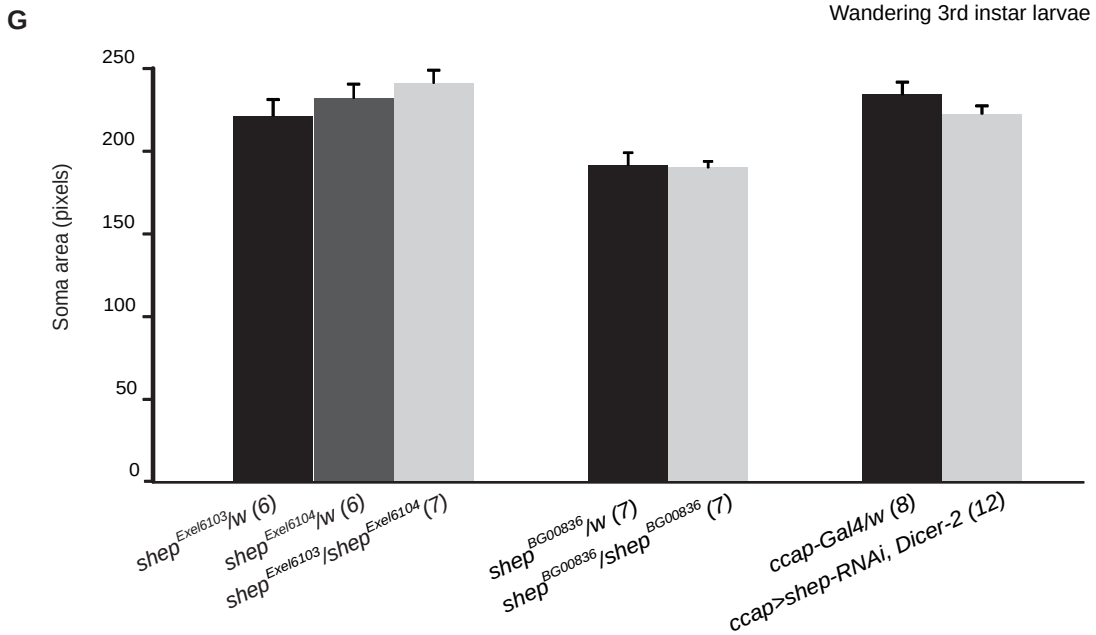

Figure S10 Loss of SHEP resulted in smaller bursicon neurons in P14 stage pharate adults but not in wandering 3rd instar larvae. (A-E) Anti-SHEP immunostaining of *shep* loss-of-function mutants at the P14 pharate adult stage. Lower SHEP levels were observed in all of the *shep* mutant backgrounds, but *elav>shep-RNAi, Dicer-2* displayed the greatest reduction of SHEP levels in the CNS. (F) In P14 stage pharate adults, we observed reduced bursicon neuron soma areas in hypomorphic *shep* mutant backgrounds, which included $shep^{Exel6103}/shep^{Exel6104}$, $shep^{BG00836}$ homozygotes, and *ccap>shep-RNAi*. (G) Bursicon neuron soma areas were unaffected in wandering 3rd larval instar *shep* mutants. The mutant backgrounds included *ccap>shep-RNAi, Dicer-2*, which was the strongest *shep* loss-of-function genotype, as judged by the impacts on branching in the peripheral axon arbor (Figure S11). The number of animals for each genotype is indicated in parentheses. **P*<0.05, ***P*<0.01, ****P*<0.001, Student's *t*-test. Scale bar: 200 µm.

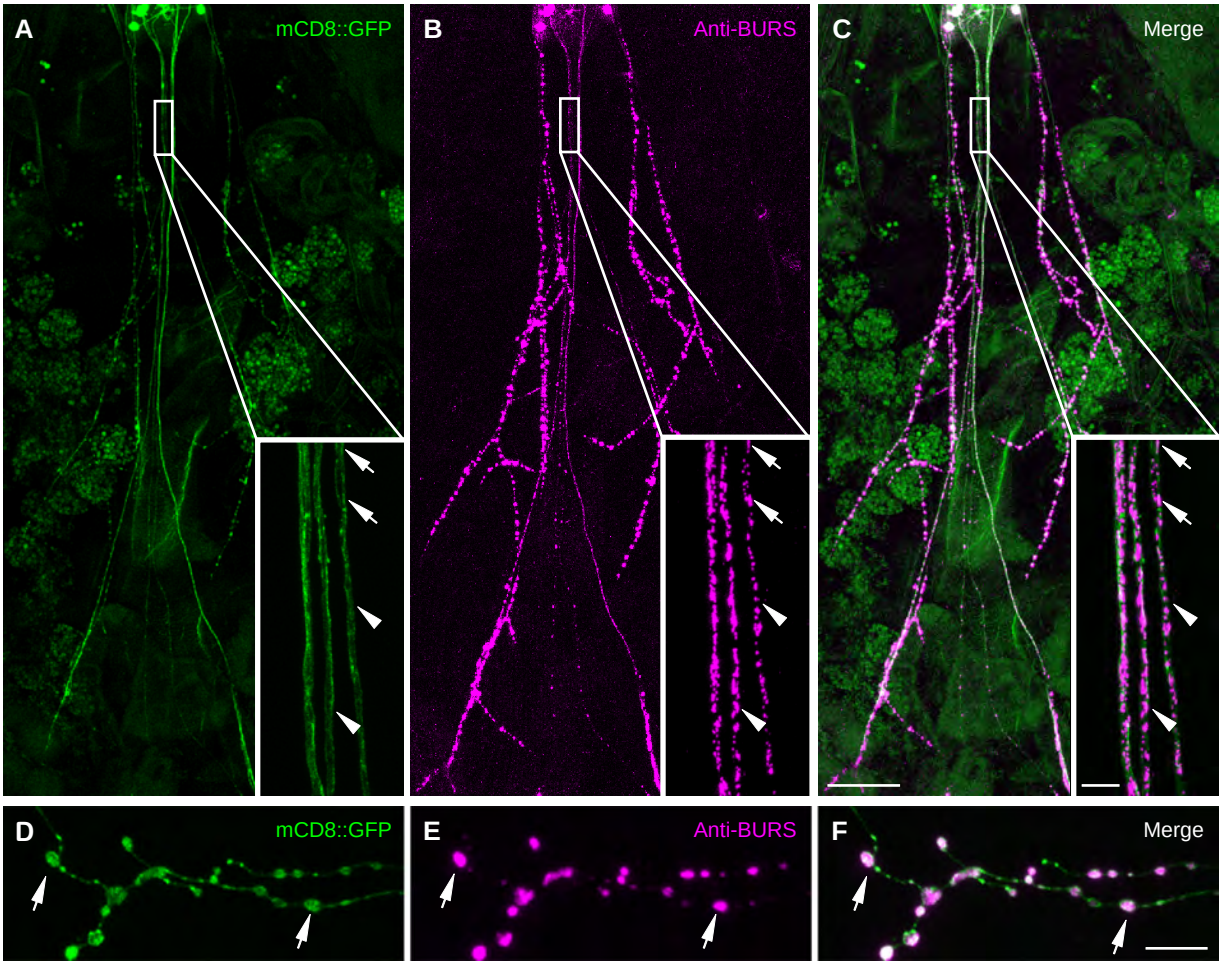

Figure S11 Bursicon neuron peripheral axon projections and synaptic terminals were visualized by anti-BURS immunostaining or genetic labeling with the membrane-localized fusion protein, mCD8::GFP. (A-C) Peripheral axons in the abdominal nerves of a *ccap>shep-RNAi, Dicer-2, mCD8::GFP* P14 stage pharate adult. Although the anti-BURS immunostaining (magenta) is more restricted to boutons than the mCD8::GFP labeling (green), each axon in the nerve can be clearly resolved at lower magnification (panels A-C), which captures most of the peripheral axon arbor, and at higher magnification (insets; region of the abdominal nerve trunk indicated by the white boxes in panels A-C). Within the abdominal nerve trunk, there is much less bursicon accumulation than in the distal boutons, but anti-BURS immunostaining still permits the visualization of each axon. Arrows, boutons; arrowheads, axons. Scale bars: A-C, 100 µm; insets, 5 µm. (D-F) Labeling of the bursicon neuron terminals on muscles 12-13 of the 2nd abdominal segment with mCD8::GFP (green) and anti-BURS immunostaining (magenta) in *ccap>shep-RNAi, Dicer-2, mCD8::GFP* wandering 3rd instar larvae. Arrows, boutons. Scale bar: 10 µm.

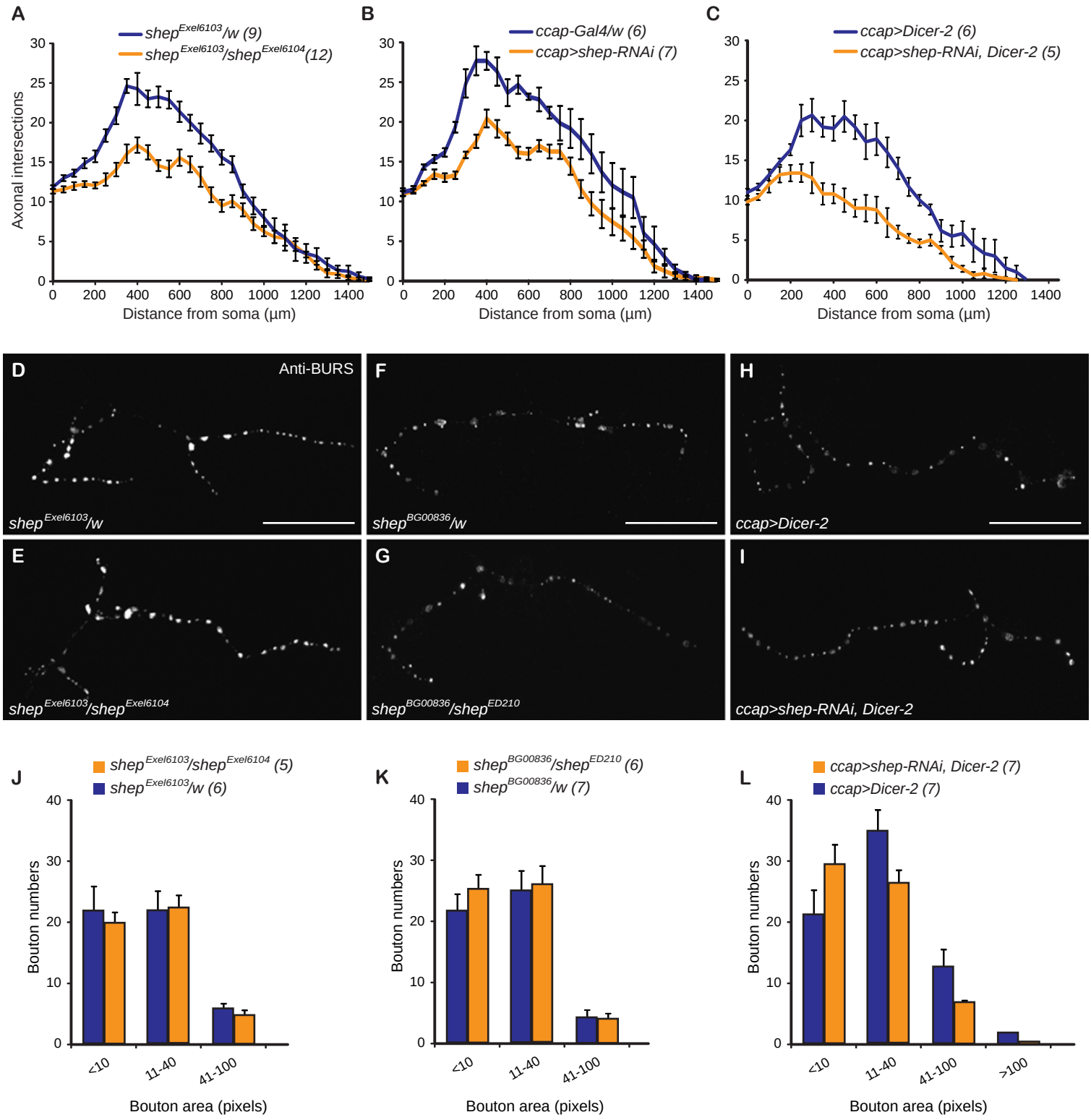

Figure S12 *shep* promoted outgrowth of the peripheral projections of the bursicon neurons during metamorphosis. (A-C) Sholl analysis on the peripheral projections of P14 stage pharate adult bursicon neurons. For this analysis, we counted the number of axon intersections with nested, concentric rings, each with a 50 µm increase in radius from the next smallest ring. Sample sizes are listed in parentheses following each genotype. (D-I) In wandering 3rd instar larvae, the morphology of the neuromuscular junctions (NMJ) of the hypomorphic mutants *shep*^{Exel6103}/*shep*^{Exel6104} (E), *shep*^{BG00836}/*shep*^{ED210}(G), and *ccap>shep-RNAi, Dicer-2* (I) was similar to the morphology of the respective hemizygous controls (D, F, and H). (J-L) Binned counts of wandering 3rd instar larval NMJ boutons within size classes for *shep* loss-of-function animals. Sample sizes are listed in parentheses. Two-way ANOVAs, P=0.452479 (panel J), P=0.597591 (panel K), and P=0.271019 (panel L). Scale bars: 100 µm.

Files S1-S5

Available for download as .avi files at http://www.genetics.org/lookup/suppl/doi:10.1534/genetics.114.166181/-/DC1

File S1 Mounting of an *Oregon R* female by an *Oregon R* virgin male. The male mounted the female shortly after copulation started, and the female extended her wings to accept the male.

File S2 Kicking of an *Oregon R* male by a $shep^{BG00836}/shep^{ED210}$ virgin female after the onset of copulation. The female continued to kick the male during copulation and did not extend her wings to accept mounting by the male.

File S3 Three-leg grooming by a $shep^{BG00836}/shep^{ED210}$ female immediately after copulation was completed. The predominant grooming pattern involved only the legs, with the two metathoracic legs rubbed together with one of the mesothoracic legs (Figure 5). Correspondingly, the proportion of time spent grooming the wings and abdomen was reduced.

File S4 Two-leg grooming of an *Oregon R* female immediately after copulation. Grooming of the wings and abdomen was performed with the two metathoracic legs.

File S5 Expulsion of what appears to be seminal fluid and the mating plug by a $shep^{BG00836}/shep^{ED210}$ female immediately after copulation. The mated $shep^{BG00836}/shep^{ED210}$ female groomed with three legs and then expelled material after ovipositor extrusion. There is a one-minute pause in the video, during which the fluid was first visible after repetitive ovipositor extrusion.